

Full Length Article

Enhanced chemical mechanical polishing (CMP) performance of porous self-assembled spherical cerium oxide via RE(La/Pr/Nd) doping



Zhenyu Zhang^{a,b,c,d}, Ning Wang^{a,b,c,d}, Xingzi Wang^{a,c,d},
 Zheng Zhao^{a,b,c}, Chen Dong^{a,b,c,e}, Xianmin Tan^{a,c,d}, Yuanyuan Zheng^{a,b,c},
 Zongyu Feng^{a,b,c,d}, Xiangxi Zhong^{a,b,c}, Juanyu Yang^{a,b,c,d,*},
 Xiaowei Huang^{a,b,c,d,*}

^a National Engineering Research Center for Rare Earth, Grirem Advanced Materials Co., Ltd., Beijing 100088, China^b Rare Earth Functional Materials (Xiong'an) Innovation Center Co., Ltd., Xiong'an 071700, China^c Grirem Hi-Tech Co., Ltd., Hebei 065201, China^d General Research Institute for Nonferrous Metals, Beijing 100088, China^e China Grimm Group Co., Ltd., Beijing 100088, China

ARTICLE INFO

Keywords:
 Chemical mechanical polishing (CMP)
 CeO_2
 Rare-Earth Doping
 Porous self-assembled spherical structures
 Density functional theory (DFT)

ABSTRACT

With the linewidth of integrated circuits has progressively narrowed, imposing higher demands on the chemical mechanical polishing (CMP) process. Cerium oxide nanoparticles are widely used as abrasives in CMP, with their physical structure and the surface content of Ce^{3+} ions and oxygen vacancies directly affecting their CMP performance. Here in, we synthesized La/Pr/Nd doped CeO_2 with the porous self-assembled spherical structures. Doping with La/Pr/Nd reduced the grain size of cerium oxide, increased its specific surface area, decreased the pore size, and increased the pore volume. HR-TEM analysis shows that the porous self-assembled spherical CeO_2 primarily exposes the (111) crystal facet. Additionally, the density functional theory (DFT) calculation, XPS, H₂-TPR and XANES analyses shown that doping of La/Pr/Nd facilitated the formation of oxygen vacancies and increased the Ce^{3+} content on the (111) crystal facet of the CeO_2 . La atoms are more likely to stabilize on the CeO_2 (111) surface compared to Pr and Nd atoms. The CMP results indicated that, The La- CeO_2 exhibited a higher MRR of $338 \pm 7.54 \text{ nm/min}$, which is a 35 % increase compared to p- CeO_2 , and achieved superior surface roughness ($R_a = 0.201 \pm 0.010 \text{ nm}$).

1. Introduction

Chemical mechanical polishing (CMP) technology is indispensable for achieving local and global planarization of semiconductor devices. It is widely utilized in polishing both optical glass and integrated circuit [1–3]. As electronic devices become increasingly integrated, the demand for the surface flatness of silicon wafers is escalating. Consequently, the importance of CMP technology is growing steadily [4]. CeO_2 is regarded as one of the most promising CMP abrasives when compared to traditional SiO_2 and Al_2O_3 [5]. This is due to its unique 4f electronic structure, as well as the coexistence of Ce^{3+} and Ce^{4+} in the crystal lattice, and the presence of inherent oxygen vacancies [6].

Due to the synergistic effect of mechanical friction and chemical reactions, CeO_2 abrasives can achieve a high material removal rate

(MRR) and high surface flatness [7]. The “Chemical Tooth” theory, originally formulated by Cook, is the mainstream theory underlying the CeO_2 polishing process [8]. Under the combined mechanical and chemical actions, the Ce^{3+} ions on the surface of cerium oxide react with the Si-O-Si or Si-OH bonds on the surface of silicon dioxide, forming Ce-O-Si bonds. the formation and breaking of Ce-O-Si bonds between CeO_2 abrasive particles and the SiO_2 film is crucial for achieving the high removal rate of cerium oxide [9,10]. Tasuku et al [11], using first-principles molecular dynamics study, discovered that during the polishing process, the formation of Ce-O-Si bonds leads to the transformation of surface Si atoms in SiO_2 into pentacoordinate Si atoms. Simultaneously, Ce^{3+} ions donate electrons to the antibonding orbitals of the Si-O bond, thereby effectively weakening or breaking the Si-O-Si bond within the pentacoordinate Si atom. Consequently, the presence of

* Corresponding authors at: National Engineering Research Center for Rare Earth, Grirem Advanced Materials Co., Ltd., Beijing 100088, China.

E-mail addresses: juanyuyang@163.com (J. Yang), hxw@grimm.com (X. Huang).

oxygen vacancies and Ce³⁺ content on the cerium oxide surface are the principal factors influencing its chemical performance during the CMP process.

Moreover, the size, morphology, and structure of cerium oxide as a polishing material have an influence on its chemical activities and mechanical properties [12–16]. Core-shell structures have been introduced into CMP due to their circular surface morphology, narrow size distribution, and low elastic modulus, resulting in effective reduction of scratch defects [17,18]. However, these structures generally exhibit low MRR and are susceptible to structural and functional failure under pressure, thus limiting their widespread application [19]. Notably, in recent years, porous spherical self-assembled cerium oxide has garnered significant attention in fields such as magnetics and catalysis due to its unique multilayered assembly structure [20,21]. In the field of CMP, Chen et al [22,23] synthesized a series of dendritic mesoporous silica (DmSiO₂) supported samarium (Sm)-doped CeO₂ nanocrystals through a simple chemical precipitation method. The resulting powders exhibited a low elastic modulus, enabling a lower surface roughness; Kim et al [24] found that spherical CeO₂ assembled from nanoparticles possesses both physically soft and chemically active (Ce³⁺ ions) properties. The spherical structure, assembled from primary particles of smaller size, possesses a higher specific surface area and a greater surface concentration of Ce³⁺ compared to single-crystal cerium oxide. Moreover, the mesopores resulting from the assembled structure contribute to a decreased elastic modulus. This results in a larger contact area with the workpiece during polishing compared to conventional single-crystal spherical cerium oxide, as well as exerting less pressure on the surface of the workpiece [16]. Consequently, it enhances the MRR while minimizing the generation of excessive scratches [25]. Furthermore, unlike core-shell structures, this structure maintains its integrity after polishing, significantly enhancing its reusability and promoting resource conservation [26]. It has been observed that in the extant literature, these spherical cerium oxide structures assembled from primary particles mainly expose the (111) crystal facet [26,27]. It is well-recognized that the cerium oxide (111) surface has the lowest concentration of surface oxygen vacancies among the major crystal facets (111/110/100), which could potentially constrain its chemical activity (Ce³⁺ ions) and become a primary limiting factor enhancements of its CMP performance [28].

The enhancement of the surface Ce³⁺ and oxygen vacancy content of cerium oxide is mainly achieved through doping with rare earth elements and transition metals, adjusting the atmosphere conditions during oxidation, and synthesizing novel structures [29–31]. Recent studies have shown significant interest in increasing the Ce³⁺ content in CeO₂ through doping aimed at enhancing the interfacial chemical reaction with SiO₂ [32–34]. Trivalent dopants, particularly those from rare earth elements, have the ability to substitute for Ce⁴⁺, leading to the release of additional oxygen vacancies and facilitating the reduction of neighboring Ce⁴⁺ ions to Ce³⁺ [35,36]. Cheng et al [37] enhanced the MRR of CeO₂ abrasives by modifying the surface of commercial particles through ion doping. Kim et al [36] synthesized La³⁺ and Nd³⁺ doped nano-cerium dioxide directly using the conventional hydrothermal method and confirmed its significant effect on improving the CMP performance of SiO₂. Preliminary studies using Density Functional Theory (DFT) calculations indicate that doping ceramic materials with rare earth elements such as La, Pr, and Nd tends to localize on the surface, decrease the formation energy of oxygen vacancies, and enhance their surface chemical activity [38].

Inspired by the considerations mentioned above, we propose a novel strategy building on the synthesis of porous spherical self-assembled cerium oxide, to enhance the surface concentrations of Ce³⁺ and oxygen vacancies by doping with La, Pr, and Nd. This strategy is expected to reduce the grain size, increase the specific surface area and pore volume, and improve the chemical and mechanical properties of CeO₂ abrasives during the CMP process. The synthesized materials were characterized by techniques such as X-ray diffraction (XRD), transmission electron

microscopy (TEM), X-ray photoelectron spectroscopy (XPS), and X-ray absorption near edge structure (XANES). The results showed that the synthesized self-assembled porous spherical cerium oxide primarily exposes the (111) crystal facet. Further, BET analysis showed that porous spherical self-assembled cerium oxide has a reduction in pore size and an increase in pore volume, as well as enhanced concentrations of surface Ce³⁺ ions and oxygen vacancies. H₂-TPR demonstrated that doping cerium oxide with La, Pr, and Nd increased the concentration of oxygen vacancies, with La doping exhibiting the highest concentration. Density functional theory (DFT) calculations further validated that doping with La/Pr/Nd reduces the formation energy for oxygen vacancies and increases oxygen vacancies on the CeO₂ (111) crystal facet. The doping formation energy indicates that La/Pr/Nd are readily distributed on the surface of cerium oxide, with La exhibiting greater stability on the surface compared to Pr and Nd. CMP tests revealed that the doped self-assembled spherical cerium oxide had a higher MRR and improved surface flatness, with La doping showing the most superior CMP performance.

2. Experimental

2.1. Materials

Cerium chloride solution was prepared by dissolving Cerium(III) chloride heptahydrate (CeCl₃·7H₂O, Aladdin, ≥ 99.9 %) in deionized water. Sodium bicarbonate solution was prepared by dissolving sodium bicarbonate ((NaHCO₃, Xilong Science Co., Ltd, ≥ 99.5 %) from General Reagent in deionized water. All chemical reagents were used as received, without additional purification.

Initially, 150 mL of 0.6 mol/L sodium bicarbonate solution was mixed with 100 mL 0.6 mol/L cerium chloride solution, resulting in a white precipitate. The molar ratio of sodium bicarbonate to the cerium chloride was denoted to R, where R = 3. The precipitate was continuously stirred at a rate of 400 rpm for 5 min, then transferred to the Teflon-lined stainless-steel autoclave, and maintained at 180 °C with continuous mixing of 300 rpm to ensure the uniform nanoparticles growth. After heating for 12 h, filter the obtained sedimentation products, wash them with deionized water and ethanol several times and dry them for 12 h at the 60 °C. Subsequently, the dried sample was heated at 900 °C, and cooled to room temperature over 3 h. Pure CeO₂ particles (p-CeO₂) were obtained. The synthesis method of La/Pr/Nd doped CeO₂ particles (La/Pr/Nd-CeO₂) followed the aforementioned procedure. In this study, lanthanide chloride salts were added to the cerium chloride solution. Lanthanum chloride heptahydrate (LaCl₃·7H₂O, Aladdin, ≥ 99.9 %), neodymium chloride hexahydrate (NdCl₃·6H₂O, Aladdin, ≥ 99.9 %), and praseodymium chloride hexahydrate (PrCl₃·7H₂O, Aladdin, ≥ 99.9 %) were utilized as precursor salts for doping with rare earth elements. The doping concentration was 10 wt%.

2.2. Characterizations

Inductively coupled plasma atomic emission spectroscopy (ICP-AES) analysis was performed with a Profile Spec ICP-AES spectrometer (Leeman, U.S.A.). The phase composition of the products was characterized by powder X-ray diffractometer (XRD, Smart-lab, Tokyo, Japan) equipped with Cu-K α radiation. The morphologies and size of the products were analyzed using offline scanning electron microscopy (SEM, JSM-7900F, JEOL, Japan). The morphology was characterized by Transmission electron microscopy (TEM, Talos F200X, Thermo Fisher Scientific, USA). The valence states of Cerium (Ce³⁺/Ce⁴⁺) were characterized using X-ray photoelectron spectroscopy (XPS, NEXSA, Thermo Scientific, USA) with an energy-dispersive X-ray spectrometer (EDS, Link ISIS, Oxford, UK). The Brunauer–Emmett–Teller surface area, pore volume and size were tested by (ASAP 2460, Micromeritics, USA). Hydrogen temperature-programmed reduction (H₂-TPR) was performed by TP-5080B, Raman spectroscopy analyses were performed on a Raman

spectroscope (ThermoFisher, Dxr2xi, UK) with an excitation laser wavelength of 532 nm in the range of 200–1200 cm⁻¹. X-ray absorption near edge structure (XANES) measurements were carried out at the X-ray adsorption spectra (XAES) station (BL14W1) in the Shanghai Synchrotron Radiation Facility (SSRF), China.^[16] The surface elastic modulus of the porous CeO₂ particles was directly tested by atomic force microscopy (AFM, Cypher S/Oxford Instruments Asylum Research) using the mode of AM-FM. Force spectroscopy tests were performed on the AFM (Cypher S/Oxford Instruments Asylum Research). The probe tip is silicon with a force constant with the set point of 800 mV (in the form of potential) and is very sharp with a curvature radius of about 2 nm, which can detect nanoscale heterogeneity.

2.3. DFT calculations

The first-principles calculation based on the Density Functional Theory (DFT) was conducted using the Vienna Ab-initio Simulation Package (VASP) code^[39]. The electronic wave functions were described using the Projector Augmented Wave (PAW) method. the cutoff energy of the plane wave basis was set to 450 eV^[40]. the Kohn-Sham equations were solved with the generalized gradient approximation (GGA), and the exchange correlation functional of Perdew-Burke-Ernzerhof (PBE) Effective Hubbard parameters (U) was employed to explain the strong on-site Coulomb repulsion between localized 4f orbitals of lanthanide elements^[38]. In this study, U=5 eV was applied to the 4f orbitals of Ce and dopants, while U=4.5 eV is applied to the 4f orbitals of Pr^[41]. In this study, we investigated the impact of La/Pr/Nd doping on the oxygen vacancies of the CeO₂ (111) surface. A 3 × 3 CeO₂ (111) slab model was constructed, and La/Pr/Nd doping was implemented by replacing Ce atoms to simulate La/Pr/Nd-CeO₂ (111). Subsequently, one oxygen atom was removed to generate an oxygen vacancy. Self-consistent calculations were performed using a 3 × 3 × 1 k-point sampling of the Brillouin zone. Structural relaxation was achieved using the Hellmann-Feynman approximation, with atomic positions relaxed until the force acting on each atom was below 0.02 eV/Å.

2.4. CMP test

2 inches silicon wafer with a 2 μm thick SiO₂ film was polished using a ProLap-15 polishing machine (Shenzhen Mayor Yong precision Technology). The basic parameter of CMP is shown in Table S1. The weight of SiO₂ film was measured using a precise balance (Mettler Toledo, CH) to calculate the MRR according to Eq. (1)

Here, Δm (g) represents the mass change of SiO₂ film before and after polishing, where M (g) denotes the mass of SiO₂ film before polishing, H (mm) signifies the thickness of SiO₂ film before polishing, t (min) indicates the polishing time, and MRR denotes the material removal rate of SiO₂ film. The MRR were calculated from three runs.

$$\text{MRR} = \frac{10^6 \times \Delta m \times H}{M \times t} \quad (1)$$

The high-resolution surface morphologies of SiO₂ film before and after polishing were characterized using atomic force microscopy (AFM, Dimension Icon, Bruker) with a scanning range of 5 × 5 μm² (512 pixels per line) in tapping mode. The recorded data were processed using the software (NanoScope Analysis) to determine the three-dimensional (3D) images and the average roughness (Ra). The presented data (average surface roughness and its standard deviation) were calculated from three runs.

Polishing slurries were prepared with the p-CeO₂, La/Pr/Nd-CeO₂, CeO₂ (Dalian Guomao Material Technology Co., Ltd) composite abrasives at a concentration of 1.0 wt% in deionized water. These slurries were then modified through pH adjustment 6.0 and surfactant (PVP, 0.5 wt%). The dispersant aimed to enhance the dispensability of the abrasives in polishing slurries. The Zeta potential of CeO₂ slurry was measured by a laser zeta potential analyzer (90Plus PALS, Brookhaven,

USA).

3. Result and discussion

3.1. Morphology and structure characterization of the La/Pr/Nd-CeO₂

The content of the dopant elements (La/Pr/Nd) in the La/Pr/Nd-CeO₂ was analyzed using ICP. The content of La, Pr, and Nd after doping is shown in Table S2, at approximately 10 %. Consistent with the doping levels designed in the experiment. Fig. 1(a, b) displays the XRD pattern of the pure CeO₂ (p-CeO₂) and La/Pr/Nd-CeO₂, demonstrating a typical cubic fluorite structure without phase separation, which aligns well with the PDF#34–0394. The diffraction peak intensities of the (111) and (220) crystal facet of La/Pr/Nd-CeO₂ have decreased to varying degrees and shifted due to lattice distortion induced by the introduction of La/Pr/Nd. According to the Debye-Scherrer equation, the grain size can be calculated based on the full width at half maximum (FWHM) and Bragg angle of the (111) and (220) diffraction peaks^[42]. Furthermore, lattice parameters can be calculated using the Bragg equation^[43]. The calculated grain sizes and lattice parameters are presented in Table 1. Following doping, the grain size of La-CeO₂ (21.4 nm), Pr-CeO₂ (26.1 nm), and Nd-CeO₂ (24.2 nm) has decreased to varying degrees compared to p-CeO₂ (30.1 nm), likely due to dopant-induced lattice distortion, which hinders grain growth. Due to the larger ionic radii of La³⁺ (1.06 Å), Pr³⁺ (1.01 Å), and Nd³⁺ (0.99 Å) compared to Ce⁴⁺ (0.92 Å), the lattice constant of La-CeO₂ (5.4395 Å), Pr-CeO₂ (5.4185 Å), and Nd-CeO₂ (5.4331 Å) have increased compared to p-CeO₂ (5.4112 Å). The variation in lattice constant after Pr doping is minor, possibly due to the oxidation Pr³⁺ to Pr⁴⁺ during calcination, where the radius of Pr⁴⁺ (0.90 Å) is slightly smaller than that of Ce⁴⁺. Additionally, when trivalent ions (La³⁺/Pr³⁺/Nd³⁺) replace Ce⁴⁺ ions, oxygen vacancies are generated to neutralize the charge, and two adjacent Ce⁴⁺ ions will transform into Ce³⁺, with a radius of 1.03 Å. This also induces significant lattice distortion, hindering crystal growth. Self-assembled spherical cerium oxide is constructed from primary particles. Doping reduces the size of these grains, which in turn affects the specific surface area of the assembled cerium oxide. The porous structures of the samples were revealed by N₂ adsorption/desorption measurements (Fig. 1 c-d). Specific surface area measurements indicate that doping with La/Pr/Nd (La-59.14 m²/g, Pr-38.25 m²/g, Nd-53.02 m²/g) resulted in an increase in surface area compared to the undoped value of 28.09 m²/g. Among these, La-CeO₂ exhibited the highest specific surface area, primarily due to lattice distortions caused by La doping, which impeded the growth of the grain size of cerium oxide, providing a larger surface area for the assembled cerium oxide. At the end of the hydrothermal preparation, the precipitate forms self-assembled spherical cerium carbonate. During the thermal decomposition of the cerium carbonate into p-CeO₂, the generated CO₂ leads to the formation of mesopores on the surface and within the p-CeO₂. Pore size and pore volume measurements indicated reductions in pore size post-doped with La, Pr, and Nd (La-4.49 nm, Pr-11.82 nm, Nd-5.65 nm) compared to undoped (14.23 nm), while pore volumes increased (La-0.115 cm³/g, Pr-0.094 cm³/g, Nd-0.105 cm³/g) from the undoped value (0.079 cm³/g). The reduction in grain size after doping resulted in decreased pore size, requiring more primary crystallites for assembly when particle sizes are similar, which increased the number of mesopores between the grains and thus led to an increase in pore volume.

SEM images of cerium oxide before and after doping are depicted in Fig. 2(a-h). Both before and after doping, the Cerium oxide particles retain a spherical morphology, are assembled from nanoparticles, possess numerous mesopores, and are evenly dispersed. The doping of elements did not significantly alter the morphology of the particles. In Fig. 2(i-l), particle size analysis was conducted, revealing that the average particle size of the doped, self-assembled cerium oxide particles remained approximately 200 nm.

Fig. 3(a) presents the TEM and HR-TEM images of p-CeO₂ particle,

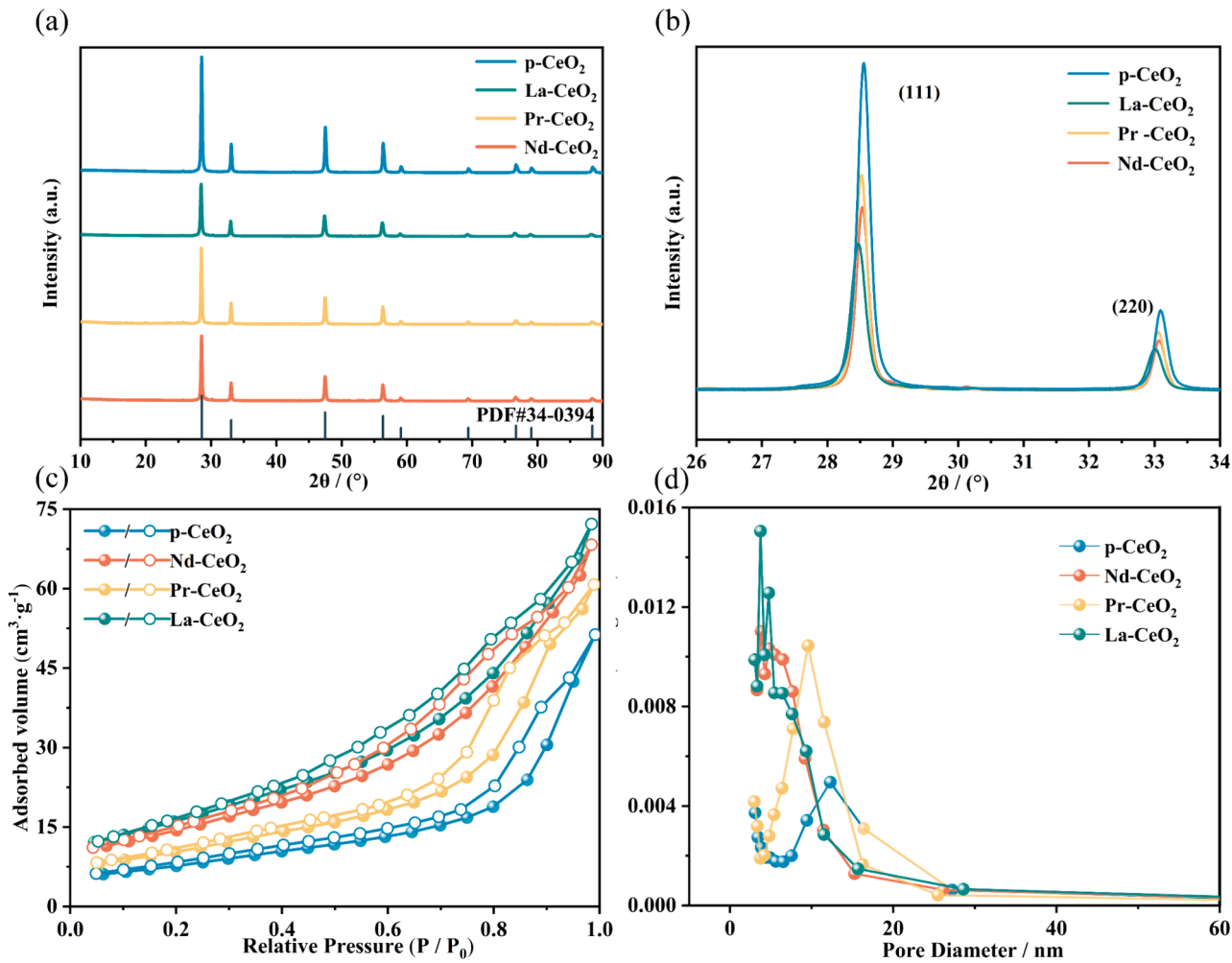


Fig. 1. (a, b) XRD patterns of p-CeO₂ and La/Pr/Nd-CeO₂; (c) N₂ adsorption/desorption isotherms of p-CeO₂ and La/Pr/Nd-CeO₂; (d) pore size distributions of p-CeO₂ and La/Pr/Nd-CeO₂.

Table 1
Lattice constant and average grain size of p-CeO₂ and La/Pr/Nd-CeO₂.

Lattice	p-CeO ₂	La-CeO ₂	Pr-CeO ₂	Nd-CeO ₂
Average grain size (nm)	30.1	21.4	26.1	24.2
Lattice constant (Å)	5.4112	5.4395	5.4185	5.4331

with p-CeO₂ displaying a spherical self-assembled structure and an interplanar spacing of 0.311 nm, corresponding to the (111) crystal facet of cerium oxide. Fig. 3(c-h) show the EDS mapping and HR-TEM images of doped cerium oxide particle. The morphology of the doped particles remains spherical, but with a smaller grain size and a denser assembled structure, leading to reduced pore size while noticeably increasing the pore volume. Post-doping, Ce, O, and La/Pr/Nd are uniformly distributed on the spheres. With the incorporation of La/Pr/Nd, the interplanar spacing increases (La-0.331 nm, Pr-0.322 nm, Nd-0.325 nm). Fig. 3(b) illustrates the La/Pr/Nd doped-CeO₂ particle schematically, showing the surface distribution of mesopores. The porous structure results in a reduced modulus of elasticity for the particles. Fig. S1 exhibits the elastic modulus mapping of the La- CeO₂ by AM-FM[44]. The average elastic modulus of La-CeO₂ is 126.45 GPa, and exhibits homogeneous distribution of the elastic modulus. Lower than the elastic modulus reported for CeO₂ (264 GPa, Nanoindentation technique; 174 GPa, Small Punch) in literature[45]. This could lead to the particles exhibiting better mechanical performance during the CMP process.

3.2. Influence of La/Pr/Nd-CeO₂ on oxygen vacancy and Ce³⁺/Ce⁴⁺ content

Fig. 4(a) depict broad-scan XPS spectrum of doped cerium oxide. The presence of dopant elements La/Pr/Nd within the cerium oxide powder is clearly evident, as indicated by characteristic XPS peaks. The surface composition of element oxides calculated from normalized peak areas in XPS spectra is summarized in Table S3. A comparison of the surface percentage content of La/Pr/Nd reveals that the surface La content (16.82 %) of doped cerium oxide is significantly higher than that of Pr (14.02 %) and Nd (13.56 %). Fig. 4(b) displays the Ce 3d XPS spectra of p-CeO₂ and La/Pr/Nd-CeO₂. The Ce 3d XPS spectra are complex, with each spectrum potentially deconvoluted into ten peaks belonging to two multiplets[46]. Specifically, the Ce 3d peaks consist of ionizations corresponding to Ce 3d_{5/2} and Ce 3d_{3/2}. Among these peaks, v₀, v', u', and u₀ peaks represent the characteristics of Ce³⁺, while v, v'', u, u'' and u''' peaks exhibit the Ce⁴⁺ [47]. The characteristic peaks of each sample are summarized in Table S4 for reference. The surface concentration of Ce³⁺ was determined by the following Eq. (2)-(4). where C and A represent concentration and area, respectively. Therefore, the Ce³⁺ content is calculated as the ratio of the area of Ce³⁺ to the sum of the areas of both Ce³⁺ and Ce⁴⁺ peaks. As shown in Table S5, after doping, the Ce³⁺ content significantly increases. Compared to the surface Ce³⁺ content of p-CeO₂ (26.4 %), the surface Ce³⁺ content of La-CeO₂ (37.3 %), Pr-CeO₂ (33.4 %), and Nd-CeO₂ (32.2 %) has increased. Fig. 4(c) shows high-resolution O1s spectra of both p-CeO₂ and La/Pr/Nd-CeO₂. The peak

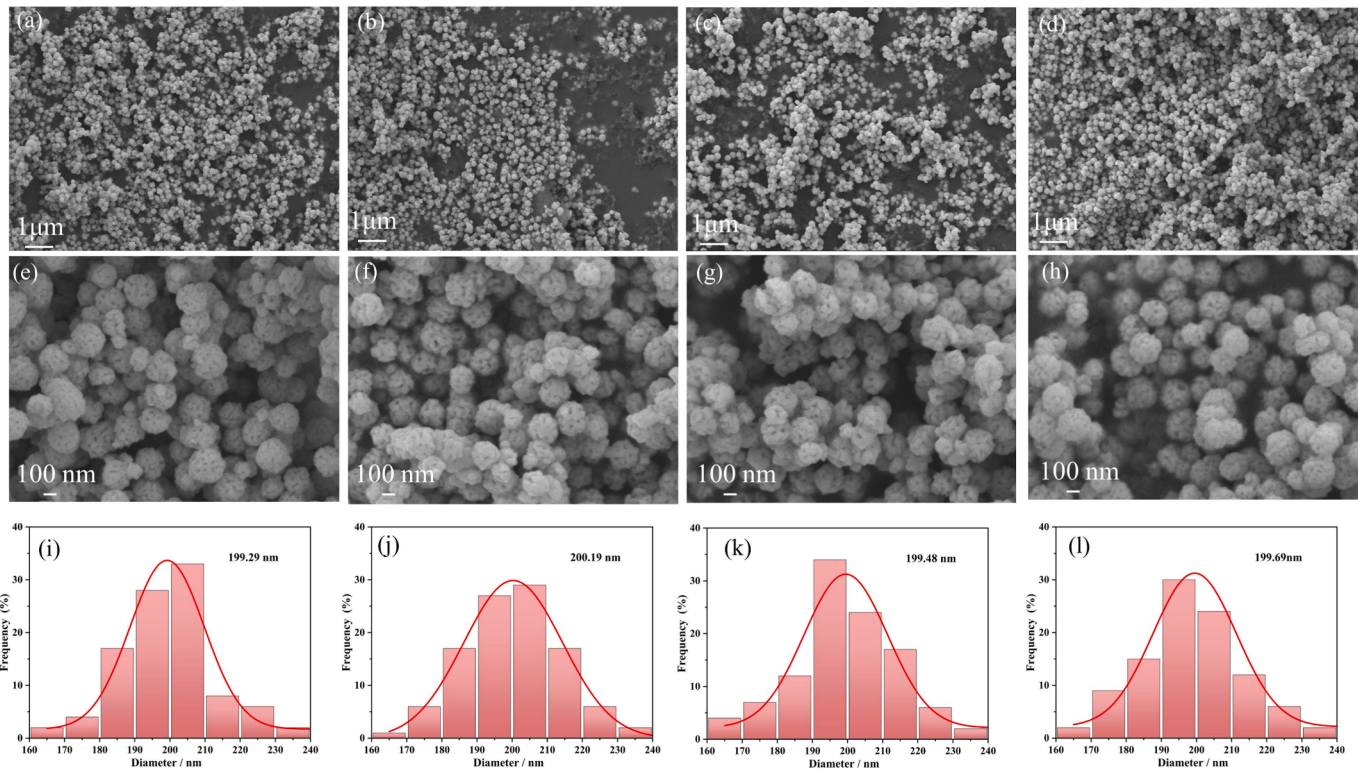


Fig. 2. SEM image of p-CeO₂ and La/Pr/Nd-CeO₂: (a, e) p-CeO₂; (b, f) La-CeO₂; (c, g) Pr-CeO₂; (d, h) Nd-CeO₂; Particle size distribution of p-CeO₂ and La/Pr/Nd-CeO₂: (i) p-CeO₂; (j) La-CeO₂; (k) Pr-CeO₂; (l) Nd-CeO₂.

at 529.3 eV corresponds to lattice oxygen (O_α), while the peak at 531.3 eV corresponds to surface oxygen (O_β). The peak at 532.2 eV is attributed to OH⁻ (O_γ) [48]. The calculation method for oxygen vacancy content (OVs) is described in Eq. (5). After doping, the oxygen vacancy content significantly increases. Compared to the surface oxygen vacancy content of p-CeO₂ (10.2 %), the surface oxygen vacancy content of La-CeO₂ (28.8 %), Pr-CeO₂ (22.4 %), and Nd-CeO₂ (21.1 %) has increased. Table S5 provides specific information on the content of Ce³⁺ ions and oxygen vacancies on the surface of the samples.

$$C(Ce^{3+}) = A(Ce^{3+}) / [A(Ce^{3+}) + A(Ce^{4+})] \quad (2)$$

$$A(Ce^{3+}) = A(v_0) + A(v') + A(u_0) + A(u') \quad (3)$$

$$A(Ce^{4+}) = A(v) + A(v'') + A(v''') + A(u) + A(u'') + A(u''') \quad (4)$$

$$C(OVs) = A(O_{\beta}) / [A(O_{\alpha}) + A(O_{\beta}) + A(O_{\gamma})] \quad (5)$$

Raman spectroscopy is the primary method for characterizing oxygen vacancies in cerium dioxide. Fig. 4(d) displays the Raman spectra of p-CeO₂ and La/Pr/Nd-CeO₂. The strongest peak, F_{2g}, appears at 465 cm⁻¹, attributed to the symmetric stretching of cerium oxide. This peak is highly sensitive to defects in cerium oxide [49]. The presence of doping elements La/Pr/Nd induce changes in the vicinity of oxygen atoms around Ce atoms in the cubic fluorite structure of cerium oxide, resulting to the formation of oxygen vacancies. Doping with La/Pr/Nd results in a red shift of the F_{2g} peak, indicating the presence of oxygen vacancies in the bulk phase, along with the reduction of Ce⁴⁺ to Ce³⁺. Within the range of 500 cm⁻¹ to 650 cm⁻¹, two minor peaks are also observed. The appearance of the α peak at 560 cm⁻¹ is indicative of oxygen vacancies, that attributed to the substitution of trivalent rare earth ions (La/Pr/Nd) into the cerium oxide lattice, and peaks near 600 cm⁻¹ are indicative of oxygen vacancies [17,50,51]. La-CeO₂ demonstrates the highest concentration of oxygen vacancies, followed by Pr-CeO₂ and Nd-CeO₂, all exceeding that of p-CeO₂. This finding is

consistent with the analysis of O 1s in XPS. As shown in Fig. 4(e), we performed XANES on p-CeO₂ and La/Pr/Nd-CeO₂ to further determine the impact of introducing dopant elements on the cerium valence state [52–54]. It was observed that the energy of the Ce L₃-edge in La/Pr/Nd-CeO₂ is lower than that in p-CeO₂ but higher than in Ce₂(CO₃)₃·6H₂O. This indicates that the valence state of Ce lies between Ce⁴⁺ and Ce³⁺. Additionally, the L₃-edge energy of Ce in La-CeO₂ is lower than in Pr-CeO₂ and Nd-CeO₂, suggesting that the cerium valence state in La-CeO₂ is lower than in Pr-CeO₂ and Nd-CeO₂. To gain a more comprehensive understanding of the chemical activity of La/Pr/Nd-CeO₂ in this study, H₂-TPR is also employed [55]. We further conducted H₂-TPR analysis. As shown in Fig. 4(f), CeO₂ samples are typically divided into three regions: Region I, Region II, and Region III. Region I and Region II correspond to temperatures between 200 °C and 650 °C, while Region III corresponds to temperatures between 650 °C and 900 °C. Previous studies suggest that Region I and Region II relate to the reduction of surface oxygen, whereas Region III pertains to the reduction of lattice oxygen in the bulk phase [56]. Specifically, Region I corresponds to the reduction of adsorbed surface oxygen, whereas Region II corresponds to the reduction of surface lattice oxygen [57]. Within Region I, La-CeO₂ displays the highest adsorbed oxygen content, correlating with a higher concentration of surface oxygen vacancies. Intriguingly, the emergence of a minor peak for Pr-CeO₂ at 381 °C implies the existence of potentially more active cerium oxide, which could impact the performance in subsequent polishing CMP processes. In Region II, p-CeO₂ did not exhibit a signal peak, thus we deduced that the signal peak around 580 °C in Region II was induced by the doping elements. La-CeO₂ exhibited greater H₂ consumption, potentially associated with the surface enrichment of La detected in XPS analyses. The elevated surface La content leads to more surface oxygen vacancies. Within Region III, the signal peak of La/Pr/Nd-CeO₂ appears at 692 °C, preceding that of p-CeO₂ (778 °C), signifying heightened activity resulting from dopant-induced lattice distortion and the presence of oxygen vacancies in the cerium oxide bulk phase. The consumption of H₂ during the H₂-TPR

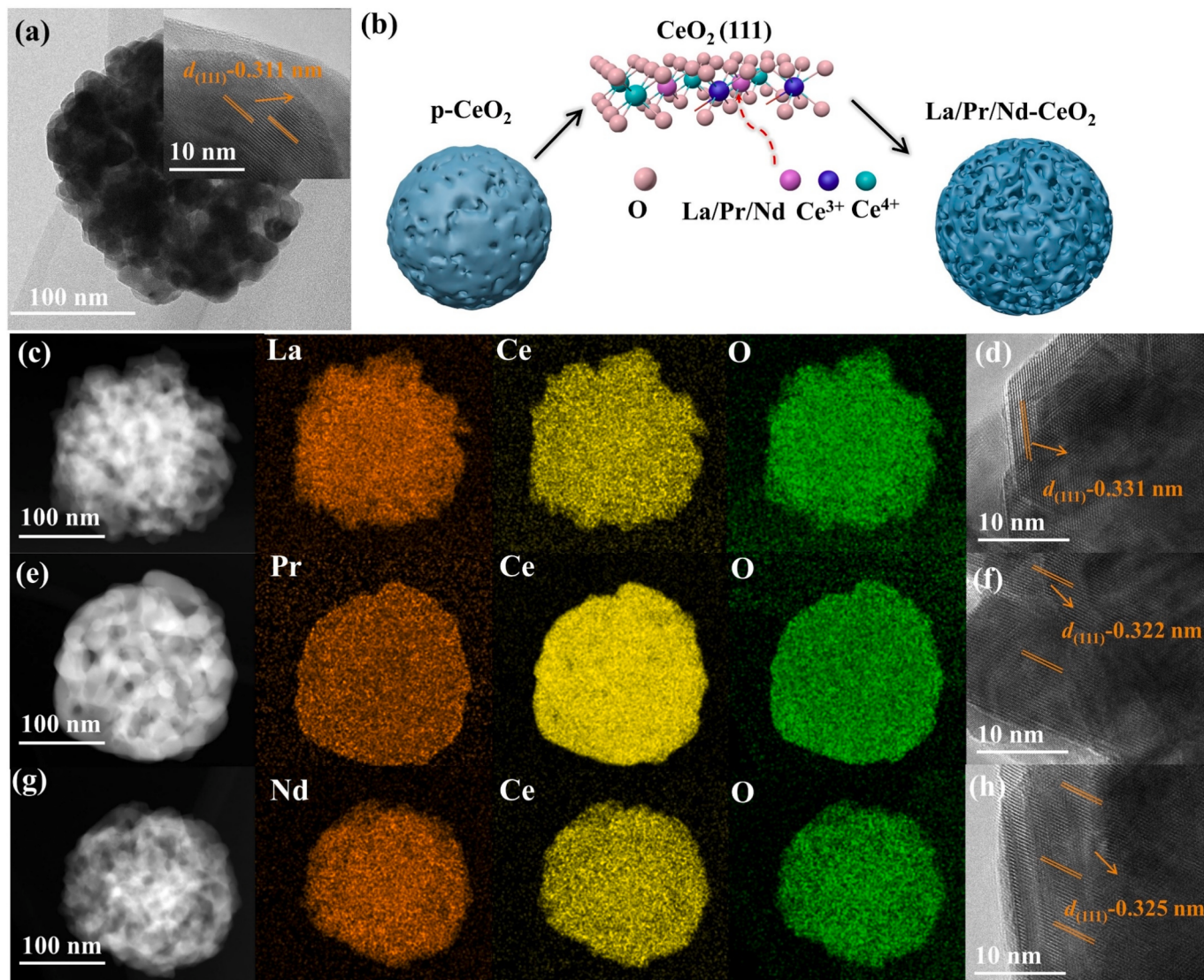


Fig. 3. (a) TEM and HR-TEM image of p-CeO₂; (b) Mechanism of Transformation in Doped Self-Assembled Porous Cerium Oxide; EDS mapping and HR-TEM of La/Pr/Nd-CeO₂; (c, d) La-CeO₂; (e, f) Pr-CeO₂; (g, h) Nd-CeO₂.

process from 200 °C to 900 °C is illustrated in Table S6, compared to the H₂ consumption of p-CeO₂ (719.55 μmol/g), the H₂ consumption of La-CeO₂ (1302.44 μmol/g), Pr-CeO₂ (989.39 μmol/g), and Nd-CeO₂ (936.88 μmol/g) is higher, with La-CeO₂ displaying the highest H₂ consumption, implying potentially superior performance in CMP processes.

According to previous studies, the (111) crystal facet of cerium oxide exhibits the highest stability[58]. Furthermore, as depicted in Fig. 3, both the p-CeO₂ and La/Pr/Nd-CeO₂ synthesized in this study predominantly expose the (111) crystal facet. The lower formation energy of oxygen vacancies leads to a more formation of oxygen vacancies. The formation of oxygen vacancies leads to the reduction of adjacent two Ce⁴⁺ ions to Ce³⁺, thus facilitating the formation of Ce³⁺ on the surface of CeO₂ [59]. Fig. 5(a, b) and Fig. S2 show the slab model of the CeO₂ (111) crystal facet and doped CeO₂ (111) crystal facet. The formation energy of oxygen vacancies (E_{vac}) can be calculated using Eq. (6), where $E(\text{cell}_{\text{vac}})$ and $E(\text{cell})$ denote the energies of supercells with and without oxygen vacancies, respectively, and $E(O_2)$ represents the energy of the ground state of oxygen molecules [39]. From Table 2, it can be observed that the calculated E_{vac} for the CeO₂ (111) surface is 2.53 eV, which is similar to other calculations 2.45 eV[60]. The formation energy of oxygen vacancies on the (111) surfaces of La-CeO₂ (1.38 eV), Pr-CeO₂

(1.90 eV), and Nd-CeO₂ (2.26 eV) is lower than that of p-CeO₂ (2.53 eV). Fig. 6(a) illustrates the relationships between oxygen vacancy energies, and oxygen vacancy and Ce³⁺ concentrations for p-CeO₂ and La/Pr/Nd-doped CeO₂. After doping with La, Pr, and Nd, there is a decrease in the formation energy of oxygen vacancies, and increases in the concentrations of surface oxygen vacancies and trivalent cerium. Specifically, La-CeO₂ exhibits the lowest formation energy of oxygen vacancies, consistent with the highest oxygen vacancy and Ce³⁺ content observed in XPS. According to previous studies, doping with rare earth atoms such as La/Pr/Nd tends to stabilize on the crystal surface [61]. Formation energy can serve as a characteristic parameter for predicting the thermal stability of crystal structures [38]. We calculated the formation energies for doping the (111) surface and subsurface of La/Pr/Nd-CeO₂. Fig. 5(c, d) illustrates the atomic models constructed for the surface(f_1) and subsurface(f_2) of doped-CeO₂. The formula for calculating formation energy is given by Eq. (7), where $E_{M-\text{CeO}_2}$ and E_{CeO_2} are total energies of RE doped and stoichiometric CeO₂ (111) surface, respectively. E_{Ce} and E_M are the energies of single Ce atom and the selected metal atom. As shown in Fig. 6 (b), it is evident that the (111) surface formation energy with these doped-CeO₂ is significantly lower than that of the subsurface. The doping with La/Pr/Nd tends to concentrate on the CeO₂ (111) surface. Furthermore, after La doping, the formation energy of both the

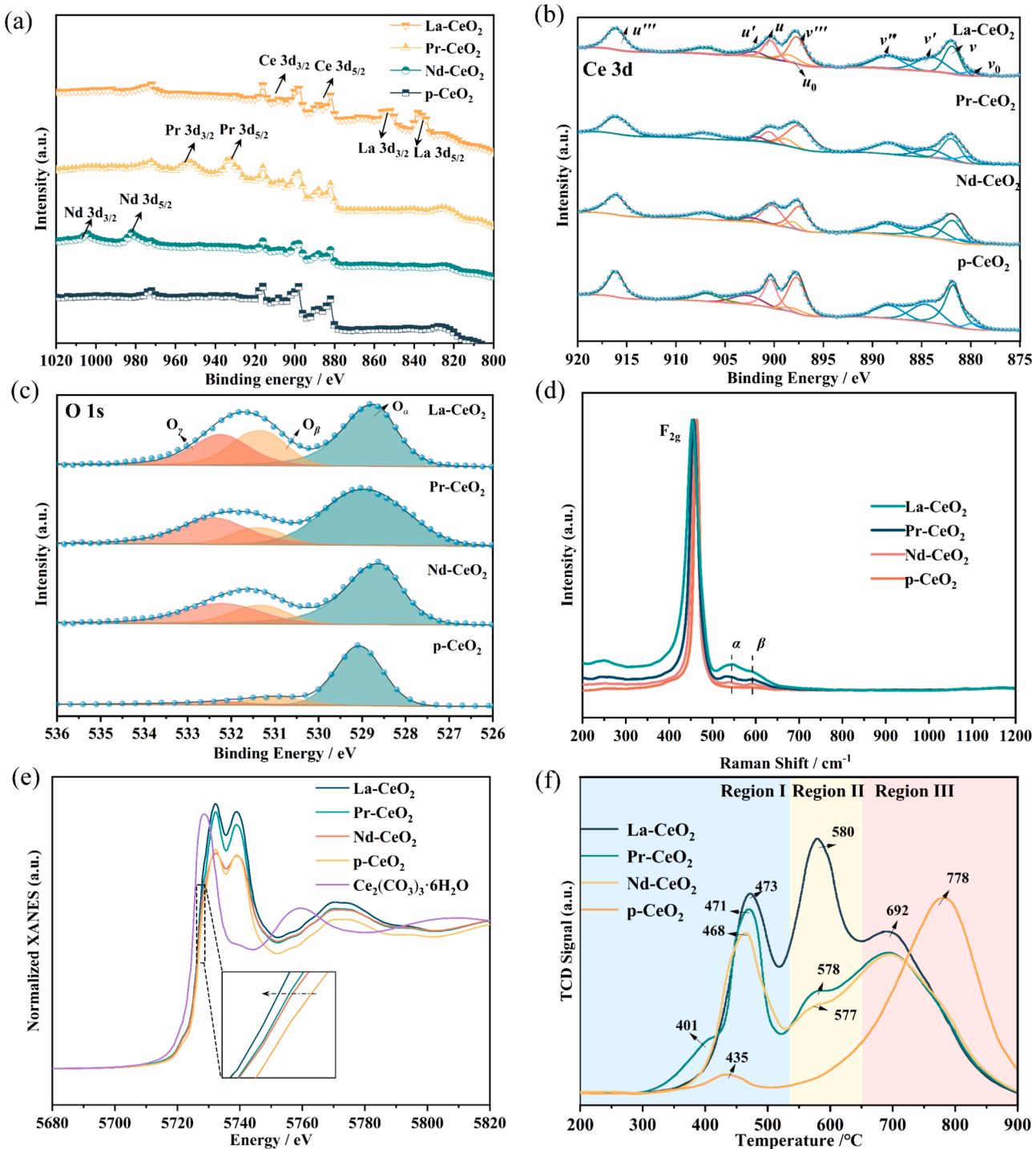


Fig. 4. (a) La, Pr, Nd, Ce binding energy ranges of p-CeO₂ and La/Pr/Nd-CeO₂; (b, c) Ce 3d and O1s p-CeO₂ and La/Pr/Nd-CeO₂; (d) Raman spectra of p-CeO₂ and La/Pr/Nd-CeO₂; (e) XANES spectra of Ce₂(CO₃)₃·6H₂O, p-CeO₂ and La/Pr/Nd-CeO₂; (f) H₂-TPR profiles of p-CeO₂ and La/Pr/Nd-CeO₂.

CeO₂ (111) surface ($E_{f1} = 0.72$ eV) and subsurface ($E_{f2} = 0.97$ eV) is the lowest in Pr-CeO₂ ($E_{f1} = 0.84$ eV, $E_{f2} = 1.22$ eV) and Nd-CeO₂ ($E_{f1} = 0.98$ eV, $E_{f2} = 1.36$ eV), indicating that La concentrates more readily on the CeO₂ (111) surface compared to Pr and Nd. This finding is corroborated by XPS results.

$$E_{vac} = E(cell_{vac}) + 1/2E(O_2) - E(cell) \quad (6)$$

$$E_f = E_{M-CeO_2} + E_{Ce} - E_{CeO_2} - E_M \quad (7)$$

3.3. CMP performance evaluations

Before conducting CMP tests, cerium oxide particles are typically formulated into a polishing slurry. As shown in the Fig. S3, the Zeta potential of the slurry prepared with our porous spherical self-assembled cerium oxide (p-CeO₂, -37 ± 2.0 mV; La-CeO₂, -43 ± 1.4 mV; Pr-CeO₂, -39 ± 1.5 mV; Nd-CeO₂, -41 ± 3.1 mV) are around -40 mV. Compared to the c-CeO₂, which has a Zeta potential of -24 ± 4.5 mV, the higher absolute value of our slurry indicates a better ability to prevent particle agglomeration. Fig. 7 illustrates the MRR data of

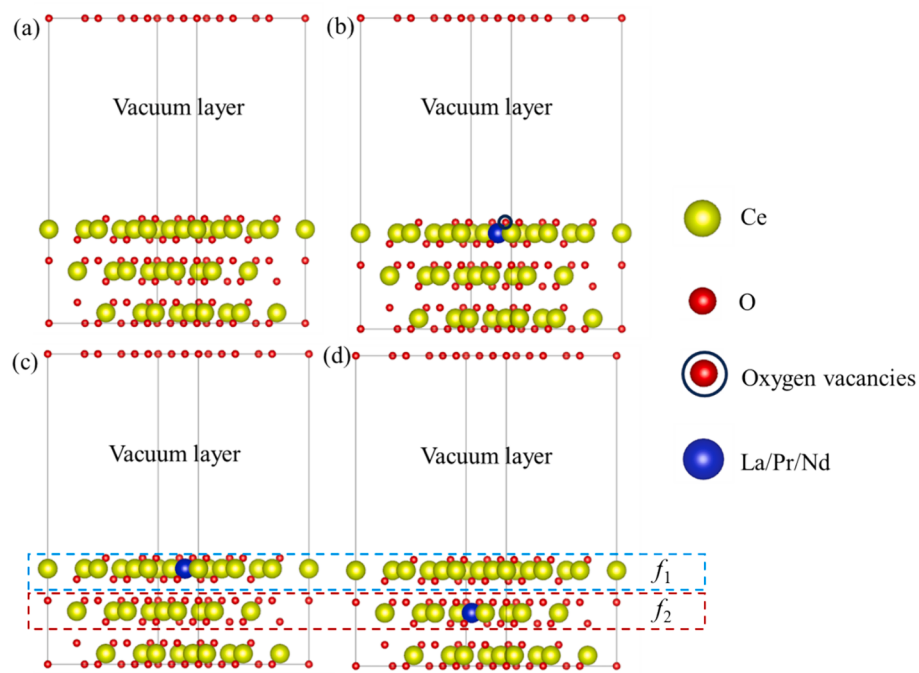


Fig. 5. (a, b) the slab model of the p-CeO₂ (111) crystal facet and La/Pr/Nd-CeO₂ (111) crystal facet; (c, d) the atomic models constructed for the surface(f_1) and subsurface(f_2) of La/Pr/Nd-CeO₂.

Table 2
The E_{vac} and formation energy (E_{f1} and E_{f2}) of RE- CeO₂ (111).

	p-CeO ₂	La-CeO ₂	Pr-CeO ₂	Nd-CeO ₂
E_{vac} (eV)	2.53	1.38	1.90	2.26
E_{f1} (eV)	--	0.72	0.84	0.98
E_{f2} (eV)	--	0.97	1.22	1.36

homemade and c-CeO₂. The MRR of the homemade powder (252 ± 6.02 nm/min) surpasses that of the c-CeO₂ (160 ± 8.18 nm/min) polishing powder. Furthermore, the MRR of La-CeO₂ (338 ± 7.54 nm/min), Pr-CeO₂ (306 ± 4.04 nm/min), and Nd-CeO₂ (295 ± 6.55 nm/min) are 20–35 % higher than that of p-CeO₂. The physical structural changes induced by doping elements, along with the increased concentrations of surface Ce³⁺ and oxygen vacancies, are the main factors that enhance the mechanical and chemical properties, leading to an increased MRR of La/Pr/Nd-CeO₂ compared to p-CeO₂. And in contrast to c-CeO₂, the enhanced MRR of homemade cerium oxide can be attributed to its

porous spherical self-assembled structure and elevated Ce³⁺ and oxygen vacancy content.

Surface roughness (R_a) after polishing is a crucial factor in assessing the effectiveness of CMP. Fig. 8(a-f) presents the 3D surface morphology of SiO₂ film before and after polishing. It can be observed that the before polished surface exhibits larger roughness, with a R_a of 0.939 ± 0.015 nm over an area of $5 \times 5 \mu\text{m}^2$. The R_a after polishing with La-CeO₂/Pr-CeO₂/Nd-CeO₂ is $0.201 \pm 0.010/0.231 \pm 0.012/0.221 \pm 0.016$ nm, lower than that achieved with p-CeO₂ ($R_a = 0.289 \pm 0.009$ nm) and c-CeO₂ ($R_a = 0.332 \pm 0.013$ nm), resulting in a smooth 3D surface morphology. Additionally, we analyzed the SiO₂ film surface before and after polishing by scanning along the dashed lines in Fig. 8(a-f) to assess the maximum asperity height, maximum valley depth, and maximum peak-to-valley distance (PV). As shown in Fig. 8(g), compared to the unpolished SiO₂ film surface and the surface polished with commercial CeO₂, the SiO₂ film surface polished with the homemade powder exhibits a more uniform distribution of roughness peaks. Both the maximum asperity height and the maximum valley depth are reduced,

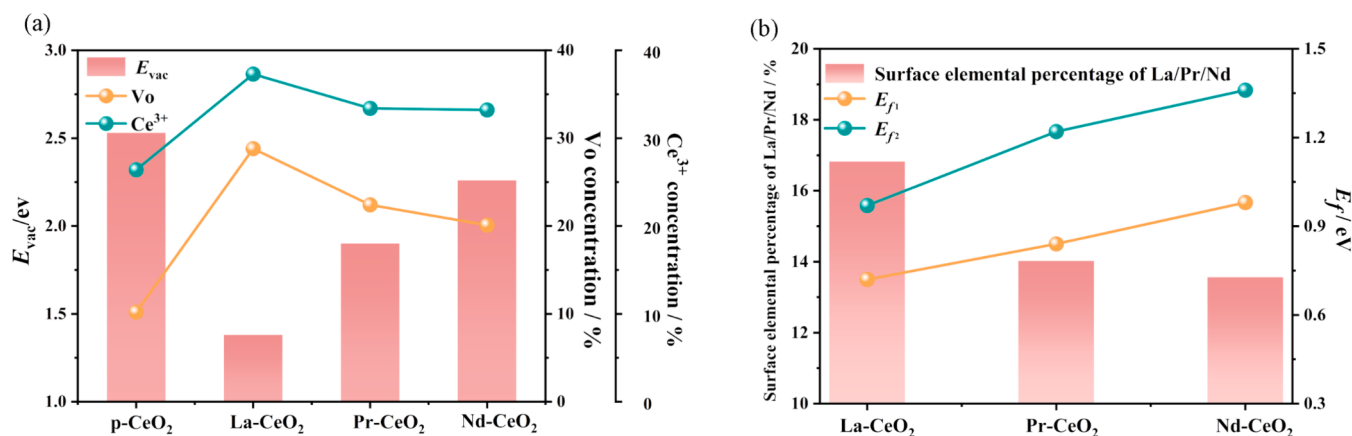


Fig. 6. (a) the oxygen vacancy energies, oxygen vacancy and Ce³⁺ concentrations for p-CeO₂ and La/Pr/Nd-CeO₂; (b)The surface elemental percentage of La/Pr/Nd, the formation energies for doping the (111) surface(f_1) and subsurface(f_2) for La/Pr/Nd-CeO₂.

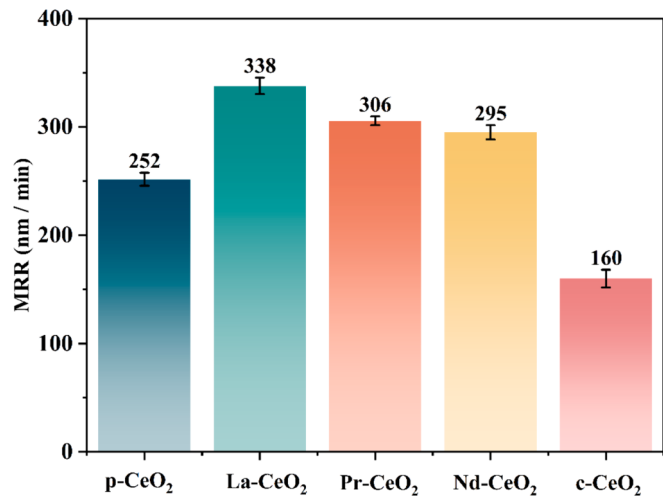


Fig. 7. The mrr of cerium oxide slurries.

with the best results observed after polishing with La-CeO₂ ($PV=0.70$ nm). Thus, porous self-assembled spherical cerium oxide particles doped with rare earth ions (La/Pr/Nd) demonstrate both a higher MRR and improved surface quality after polishing. Among them, La-CeO₂ has the best CMP performance.

As shown in Fig. S4, the CeO₂ particles did not exhibit significant morphological and structural changes after CMP, indicating that the porous spherical self-assembled structure maintains strong stability under pressure and friction. Additionally, we collected the CeO₂ slurry waste after CMP and conducted morphological and elemental analyses using TEM and EDS. As indicated by the red circles in Fig. 9 (a, e), we observed particles with irregular morphology that are distinctly different from the cerium oxide particles. The elemental mapping results, as shown in Fig. 9 (b-d, f-h), indicate that the irregular particles are composed of Si and O elements, while the regions of the porous spherical assembled particles predominantly contain Ce and O elements, with a minor presence of Si. The quantitative elemental analysis results from Fig. 9 (f-h) are presented in Fig. S5 and Table S7, showing that the irregular particles consist of 13.7 % Si, 5.47 % Ce, and 81.46 % O by atomic percentage. These findings suggest that the irregularly shaped

particles are likely lumped SiO₂. As shown in the Fig. S6, the SEM image of polished samples exhibit a smooth, mirror-like appearance with surface defects. Additionally, almost no adsorbed particles were observed on the surface.

The La/Pr/Nd-CeO₂ abrasive demonstrates excellent CMP performance. Fig. 10 illustrates the polishing mechanism of cerium oxide abrasive post-doping. In terms of mechanical action, the porous spherical structure, assembled from primary particles, exhibits two primary mechanical removal behaviors during polishing: sliding and rolling. Additionally, the porous structure results in a reduced modulus of elasticity for the particles, causing slight elastic deformation when in contact with the SiO₂ film surface. This deformation reduces the impact on the SiO₂ film surface while increasing the contact area between the particles and the SiO₂ film. This optimization in mechanical behavior can partially reduce scratches and damage [18,32]. In terms of chemical action, doping with La, Pr, and Nd increases the concentration of Ce³⁺ ions and oxygen vacancies on the surface of cerium oxide, thereby enhancing the chemical activity of La/Pr/Nd-CeO₂. Additionally, the reduction in primary particle size also leads to an increased specific surface area, which enlarges the contact area between La/Pr/Nd-CeO₂ and SiO₂ film, providing more reaction sites for the formation of Ce-O-Si bonds. In the CMP process using CeO₂ as abrasives, the key link between the structural characteristics of the abrasive and its mechanical performance is believed to be the Ce-O-Si chemical bond. Surface defects on CeO₂ particles, particularly Ce³⁺ and oxygen vacancies, facilitate the formation of Ce-O-Si bonds [62]. The removal mechanism of SiO₂ is fundamentally related to the dynamic formation and breaking of Ce-O-Si bonds, which makes the CMP process more efficient and of higher quality [63]. The Ce³⁺ and oxygen vacancy content on the surface of La/Pr/Nd-CeO₂ have significantly increased compared to p-CeO₂. Among them, La-CeO₂ has the highest content of Ce³⁺ and oxygen vacancies on the surface. The enriched surface Ce³⁺ and oxygen vacancies (OVs) facilitate the chemical bonding between cerium oxide and SiO₂, thereby enhancing the chemical reaction efficiency during the CMP process [4,23,37]. Therefore, the MRR of La/Pr/Nd-CeO₂ is superior to that of p-CeO₂. Among them, La-CeO₂ has the highest MRR. Based on the above discussion of the mechanisms, the doped porous spherical self-assembled cerium oxide prepared in this study demonstrates optimized mechanical behavior and enhanced chemical reactions during the CMP process. This results in a high MRR and superior surface quality.

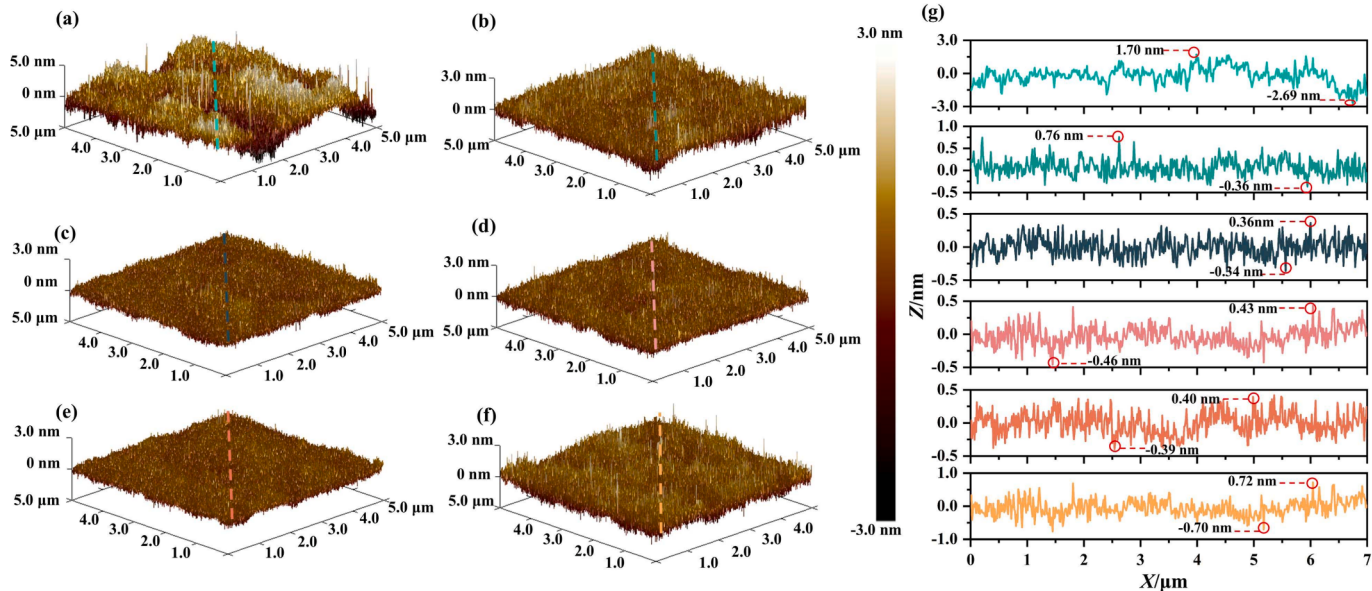


Fig. 8. AFM images of the SiO₂ film before and after polishing with different CeO₂ abrasives: (a) before polished; (b) p-CeO₂; (c) La-CeO₂; (d) Pr-CeO₂; (e) Nd-CeO₂; (f) c-CeO₂; (g) The corresponding contour line curve.

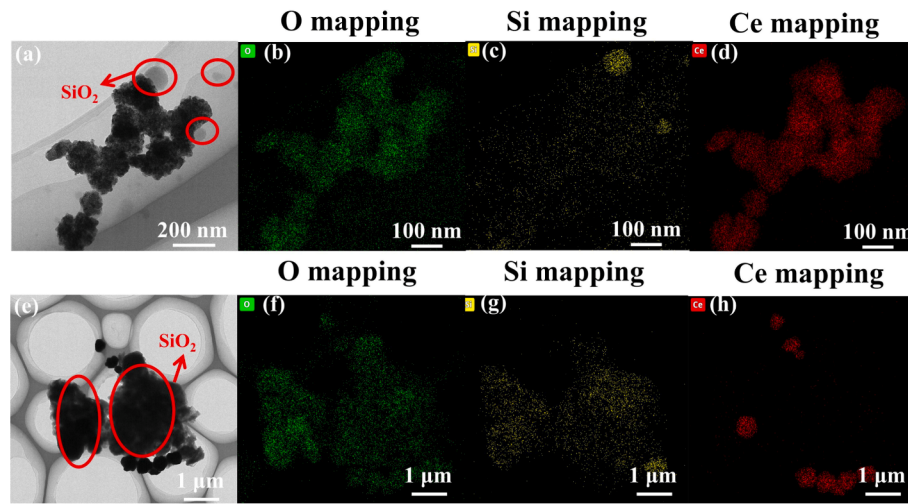


Fig. 9. (a, e) TEM image and (b-d, f-h) EDS Mapping image of CeO_2 slurry waste.

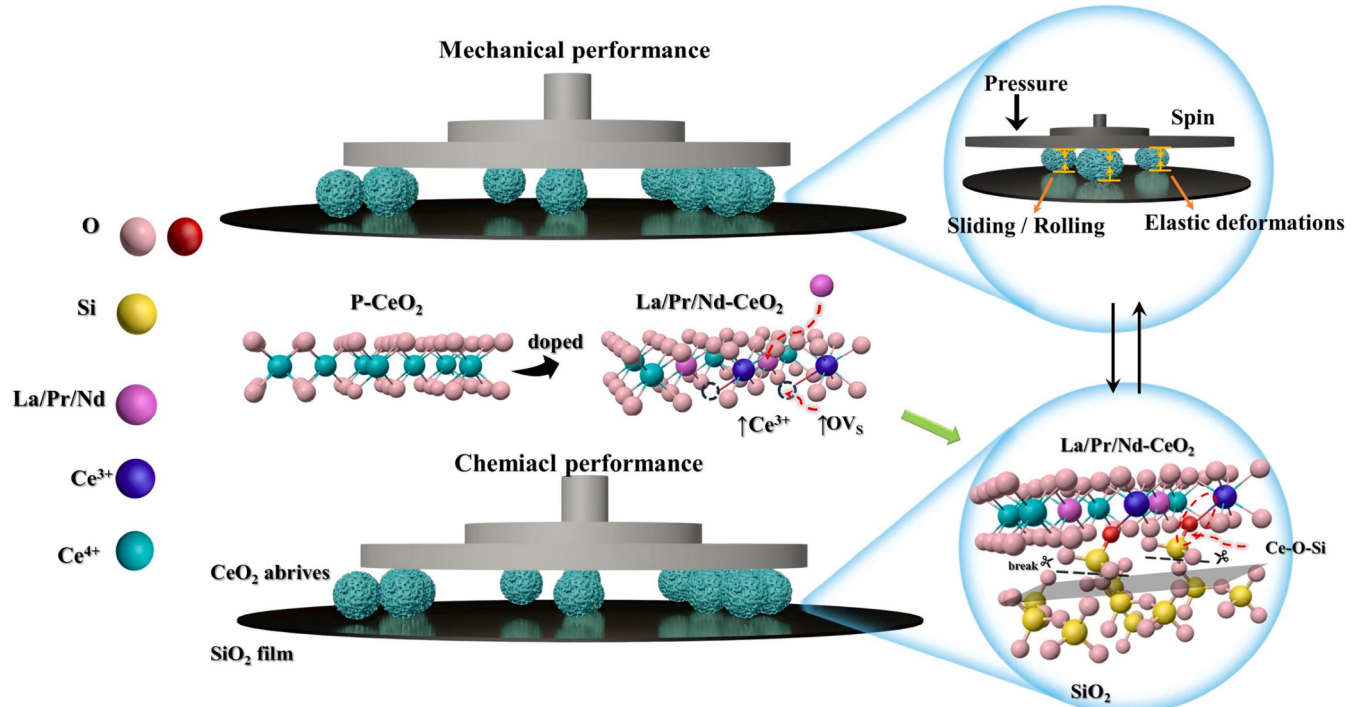


Fig. 10. Schematic of the atomic structure of RE- CeO_2 surfaces and polishing mechanism.

4. Conclusion

To enhance the CMP performance of CeO_2 abrasives, we synthesized rare earth (RE) ions (La, Pr and Nd) doped CeO_2 with the porous self-assembled spherical structures. After doping with La, Pr, and Nd, the grain size of cerium oxide particles decreases, the specific surface area increases, the pore size decreases, and the pore volume increases. Moreover, doping with La/Pr/Nd elements promotes the formation of surface oxygen vacancies and the transition of Ce^{4+} to Ce^{3+} in CeO_2 , this results in an increase in the content of surface Ce^{3+} . Among these, La doping showing the highest content of oxygen vacancies and surface Ce^{3+} . The surface Ce^{3+} content of CeO_2 doped with La/Pr/Nd is 37.3 %/33.4 %/32.2 %, significantly higher than before doping (26.4 %). DFT calculations indicate that doping with La, Pr, and Nd reduces the formation energy of oxygen vacancies on the CeO_2 (111) surface. Among

these, La doping results in the lowest oxygen vacancies formation energy, thereby facilitating their formation of oxygen vacancies. The formation energies on both the surface and subsurface of CeO_2 (111) indicate that doping with La, Pr, and Nd stabilizes easily on the CeO_2 (111) surface, with La showing higher stability and a greater tendency to be distributed on the CeO_2 (111) surface, these observations are consistent with XPS results. Compared to p- CeO_2 ($R_a = 0.289 \pm 0.009$ nm, MRR=252 ± 6.02 nm/min), the MRR and surface precision of La/Pr/Nd-doped CeO_2 have improved ($R_a = 0.201 \pm 0.010/0.231 \pm 0.012/0.221 \pm 0.016$ nm, MRR = 338 ± 7.54/306 ± 4.04/295 ± 6.55 nm/min). Owing to its higher MRR and excellent surface quality of this doped- CeO_2 abrasive, it is believed that the rare earth element-doped porous spherical self-assembled cerium oxide developed in this study will achieve large-scale application in STI polishing of advanced process integrated circuits.

CRediT authorship contribution statement

Zhenyu Zhang: Writing – review & editing, Writing – original draft, Methodology, Investigation, Funding acquisition, Formal analysis, Data curation, Conceptualization. **Ning Wang:** Software, Resources, Project administration, Investigation. **Xingzi Wang:** Writing – original draft, Investigation, Formal analysis, Data curation. **Zheng Zhao:** Software, Formal analysis, Data curation. **Chen Dong:** Visualization, Software, Formal analysis, Data curation. **Xianmin Tan:** Software, Resources, Methodology. **Yuanyuan Zheng:** Resources, Project administration. **Zongyu Feng:** Software, Resources, Investigation, Conceptualization. **Xiangxi Zhong:** Software, Resources, Funding acquisition. **Juanyu Yang:** Writing – review & editing, Writing – original draft, Software, Methodology, Funding acquisition, Formal analysis, Data curation, Conceptualization. **Xiaowei Huang:** Writing – review & editing, Writing – original draft, Validation, Supervision, Software, Project administration, Methodology, Investigation, Funding acquisition, Formal analysis.

Declaration of competing interest

The authors declare that they have no known competing financial interests or personal relationships that could have appeared to influence the work reported in this paper.

Data availability

Data will be made available on request.

Acknowledgments

This work was financially supported by the National Key Research and Development Program [No. 2021YFB3501102]. Sponsored by Beijing Nova Program [No. 20220484827]. National Natural Science Foundation of China [No. 52304370]. Central Government Guidance Local Science and Technology Development Fund Projects of Hebei Province [No. 236Z4102G]. Natural Science Foundation of Hebei Province [No. E2022103012]. The Postdoctoral Fellowship Program Grade of China Postdoctoral Science Foundation [No. GZC20233122]. The authors thank the beamline BL14W1 of Shanghai Synchrotron Radiation Facility (China) for providing the beamtime.

Appendix A. Supplementary data

Supplementary data to this article can be found online at <https://doi.org/10.1016/j.apsusc.2024.161236>.

References

- [1] X. Yuan, H. Lei, C. Chen, An ethylenediaminetetraacetic acid (EDTA) surface-functionalized CeO₂ composite abrasives with the effective improvement of the removal rate on glass CMP, Ceram. Int. 50 (2024) 293–305.
- [2] N. Xu, J. Ma, Q. Liu, Y. Luo, Y. Pu, Preparation of CeO₂ abrasives by reducing atmosphere-assisted molten salt method for enhancing their chemical mechanical polishing performance on SiO₂ substrates, J. Rare Earths 41 (2023) 1627–1635.
- [3] X. Han, R. Liu, B. Tan, F. Wang, M. Yan, X. Zhao, J. Zhao, Research progress on the application of ceria nanoparticles as abrasives in dielectric layer CMP and post cleaning: Structure, morphology, doping, and mechanism, Colloids Surf A Physicochem Eng Asp 679 (2023) 132551.
- [4] D. Datta, H. Rai, S. Singh, M. Srivastava, R.K. Sharma, N.N. Gosvami, Nanoscale tribological aspects of chemical mechanical polishing: A review, Applied Surface Science Advances 11 (2022) 100286.
- [5] H. Lee, H. Jeong, Analysis of removal mechanism on oxide CMP using mixed abrasive slurry, Int. J. Precis. Eng. Manuf. 16 (2015) 603–607.
- [6] C. Chen, Y. Cui, X. Li, S. Shen, W. Liao, H. You, Novel ceria/graphene oxide composite abrasives for chemical mechanical polishing, Ceram. Int. (2024).
- [7] K. Wakamatsu, S. Kurokawa, T. Toyama, T. Hayashi, CMP characteristics of quartz glass substrate by aggregated colloidal ceria slurry, Precis. Eng. 60 (2019) 458–464.
- [8] L.M. Cook, chemical processes in glass polishing, J. Non Cryst. Solids 120 (1990) 152–171.
- [9] Y. Guo, Z. Liu, H. Song, J. Shen, Adhesion strength and electronic properties of the interface between CeO₂ and SiO₂: First-principles calculations, Comput. Mater. Sci. 242 (2024) 113096.
- [10] L. Xie, J. Cheng, T. Wang, X. Lu, Mechanical wear behavior between CeO₂(100), CeO₂(110), CeO₂(111), and silicon studied through atomic force microscopy, Tribol. Int. 153 (2021) 106616.
- [11] T. Onodera, H. Takahashi, S. Nomura, First-principles molecular dynamics investigation of ceria/silica sliding interface toward functional materials design for chemical mechanical polishing process, Appl. Surf. Sci. 530 (2020) 147259.
- [12] T. Wang, Y. Chen, A. Chen, Y. Chen, Development of carbon sphere/ceria (CS/CeO₂) heterostructured particles and their applications to functional abrasives toward photochemical mechanical polishing, Appl. Surf. Sci. 593 (2022) 153449.
- [13] C.R. Li, Q.T. Sun, N.P. Lu, B.Y. Chen, W.J. Dong, A facile route for the fabrication of CeO₂ nanosheets via controlling the morphology of CeOHCO₃ precursors, J. Cryst. Growth 343 (2012) 95–100.
- [14] Z. Zou, W. Tian, X. Mao, J. Li, Y. Lan, C. Chen, H.Y. Sohn, J. Zhang, F. Liu, Synthesis, phase transformation and applications of CeCO₃OH: A review, J. Rare Earths. 42 (2024) 1403–1420.
- [15] Y.H. Kim, Y.G. Jung, G.S. Yoon, J. Moon, A. Watanabe, M. Naito, U. Paik, Non-Prestonian behavior of rectangular shaped ceria slurry in shallow trench isolation chemical mechanical planarization, J. Nanosci Nanotechnol 12 (2012) 2810–2814.
- [16] Z. Liu, Z. Zhang, Y. Sui, Q. Peng, J. Li, C. Shi, J. Zheng, B. Tian, Development of mesoporous abrasives and its unprecedented polishing performance elucidated by a novel atomic model, Materials Today Sustainability 25 (2024) 100700.
- [17] T. Munawar, A. Bashir, M.S. Nademe, F. Mukhtar, S. Manzoor, M.N. Ashiq, S. A. Khan, M. Koc, F. Iqbal, Core-shell CeO₂@C60 hybrid serves as a dual-functional catalyst: Photocatalyst for organic pollutant degradation and electrocatalyst for oxygen evolution reaction, Ceram. Int. 49 (2023) 8447–8462.
- [18] M. Wang, Z. Mu, T. Wang, Y. Chen, A. Chen, Double-layered core-shell heterostructures of mSiO₂@CdS@CeO₂ abrasive systems toward photochemical mechanical polishing (PCMP) applications, Appl. Surf. Sci. 614 (2023) 156274.
- [19] Y. Fan, J. Jiao, L. Zhao, J. Tang, Preparation of lanthanide-doped polystyrene/CeO₂ abrasives and investigation of slurry stability and photochemical mechanical polishing performance, Colloids Surf A Physicochem Eng Asp 656 (2023) 130508.
- [20] R. Suarez Anzorena, F.F. Muñoz, P. Bonelli, A.L. Cukierman, S.A. Larrondo, Hierarchical, template-free self-assembly morphologies in CeO₂ synthesized via urea-hydrothermal method, Ceramics International, 46 (2020) 11776–11785.
- [21] J. Li, R. He, G. Guo, Y. Li, Y. Liao, Y. Li, Synthesis of Hierarchical Layered Quasi-Triangular Ce(OH)CO₃ and Its Thermal Conversion to Ceria with High Polishing Performance, ACS Omega 8 (2023) 8519–8529.
- [22] Y. Chen, C. Zuo, Z. Li, A. Chen, Design of ceria grafted mesoporous silica composite particles for high-efficiency and damage-free oxide chemical mechanical polishing, J. Alloy. Compd. 736 (2018) 276–288.
- [23] Y. Chen, M. Wang, W. Cai, T. Wang, A. Chen, Structural regulation and polishing performance of dendritic mesoporous silica (D-mSiO₂) supported with samarium-doped cerium oxide composites, Adv. Powder Technol. 33 (2022) 103595.
- [24] K. Kim, D.K. Yi, U. Paik, Increase in Ce³⁺ Concentration of Ceria Nanoparticles for High Removal Rate of SiO₂in Chemical Mechanical Planarization, ECS J. Solid State Sci. Technol. 6 (2017) P681–P685.
- [25] P. Wu, N. Liu, X. Li, Y. Zhu, Material removal rate model for chemical-mechanical polishing of single-crystal SiC substrates using agglomerated diamond abrasive, Precis. Eng. 88 (2024) 572–583.
- [26] N.-Y. Kim, U. Hwang, J. Sung, I.-K. Park, T. Kim, J. Suhr, J.-D. Nam, Particle size dependence of nanoclustered ceria abrasives on surface activity and chemical mechanical planarization performance, Appl. Surf. Sci. (2024) 160123.
- [27] N.-Y. Kim, G. Kim, H. Sun, U. Hwang, J. Kim, D. Kwak, I.-K. Park, T. Kim, J. Suhr, J.-D. Nam, A nanoclustered ceria abrasives with low crystallinity and high Ce³⁺/Ce⁴⁺ ratio for scratch reduction and high oxide removal rates in the chemical mechanical planarization, J. Mater. Sci. 57 (2022) 12318–12328.
- [28] Y. Zhang, S. Bals, G. Van Tendeloo, Understanding CeO₂-Based Nanostructures through Advanced Electron Microscopy in 2D and 3D, Part. Part. Syst. Char. 36 (2018) 1800287.
- [29] J. Choi, D.A. Reddy, M.J. Islam, R. Ma, T.K. Kim, Self-assembly of CeO₂ nanostructures/reduced graphene oxide composite aerogels for efficient photocatalytic degradation of organic pollutants in water, J. Alloy. Compd. 688 (2016) 527–536.
- [30] A. El-Habib, B. Brioual, J. Zimou, Z. Rossi, A. Marjaoui, M. Zanouni, A. Aouni, M. Jbilou, M. Diani, M. Addou, Comparative studies on the structural, optical and electrochemical properties of Gd, Nd and In-doped CeO₂ nanostructured thin films, Mater. Sci. Semicond. Process. 176 (2024).
- [31] B. Wu, P. Wang, Y. Wang, X.-P. Qu, B. Tan, S. Hamada, Y. Wada, H. Hiyama, Removal of Nanoceria Abrasive Particles by Using Diluted SC1 and Non-Ionic Surfactant, ECS J. Solid State Sci. Technol. 10 (2021) 034010.
- [32] Y. Fan, J. Jiao, L. Zhao, J. Tang, C. Chen, N. Fan, Nd-doped porous CeO₂ abrasives for chemical mechanical polishing of SiO₂ films, Mater. Sci. Semicond. Process. 175 (2024) 108265.
- [33] N. Xu, Y. Luo, J. Ma, Y. Lin, X. Zhu, Y. Pu, Enhancement mechanism of Y-doped Ce_{1-x}Y_xO₂ for photocatalytic-assisted chemical-mechanical polishing, Mater. Today Commun. 38 (2024) 107791.
- [34] N. Xu, Y. Luo, Y. Lin, J. Ma, Y. Pu, The influence of CeO₂ abrasive size on the performance of photocatalytic assisted chemical-mechanical polishing by Y/Pr co-doping strategy, Colloids Surf A Physicochem Eng Asp 684 (2024) 133107.
- [35] C. Shuai, K. Wang, S. Peng, J. Zan, J. Xiao, S. Hu, Q. Zhong, Accelerating Ce³⁺/Ce⁴⁺ Conversion in CeO₂ via Mn doping to Endow Scaffolds with Chemodynamic Therapy Properties, Surf. Interfaces 45 (2024) 103846.

- [36] E. Kim, J. Lee, C. Bae, H. Seok, H.-U. Kim, T. Kim, Effects of trivalent lanthanide (La and Nd) doped ceria abrasives on chemical mechanical polishing, *Powder Technol* 397 (2022) 117025.
- [37] J. Cheng, S. Huang, Y. Li, T. Wang, L. Xie, X. Lu, RE (La, Nd and Yb) doped CeO₂ abrasive particles for chemical mechanical polishing of dielectric materials: Experimental and computational analysis, *Appl. Surf. Sci.* 506 (2020) 144668.
- [38] C. He, R. Sun, L. Fu, J. Huo, C. Zhao, X. Li, Y. Song, S. Wang, Defect engineering for high-selection-performance of NO reduction to NH₃ over CeO₂ (111) surface: A DFT study, *Chin. Chem. Lett.* 33 (2022) 527–532.
- [39] H.V. Thang, T.L.M. Pham, DFT insights into the electronic structure of Rh single-atom catalysts stabilized on the CeO₂(1 1 1) surface, *Chem. Phys. Lett.* 803 (2022) 139810.
- [40] D.-R. Chu, Z.-Q. Wang, X.-Q. Gong, Theoretical insights into CO oxidation activities on CeO₂(111) steps, *Surf. Sci.* 722 (2022) 122096.
- [41] B. Milberg, A. Juan, B. Irigoyen, Redox behavior of a low-doped Pr-CeO₂(111) surface. A DFT+U study, *Appl. Surf. Sci.* 401 (2017) 206–217.
- [42] J. Liu, L. Yan, X. Chen, S. Wang, M. Zhang, C.a. Tian, Direct synthesis of hollow polyhedral ceria nano powders via a template-free mixed solvothermal route, *J. Rare Earths* 33 (2015) 892–897.
- [43] T. Alammar, H. Noei, Y. Wang, W. Grüner, A.-V. Mudring, Ionic Liquid-Assisted Sonochemical Preparation of CeO₂ Nanoparticles for CO Oxidation, *ACS Sustain. Chem. Eng.* 3 (2014) 42–54.
- [44] C. Pei, S. Chen, T. Zhao, M. Li, Z. Cui, B. Sun, S. Hu, S. Lan, H. Hahn, T. Feng, Nanostructured Metallic Glass in a Highly Upgraded Energy State Contributing to Efficient Catalytic Performance, *Adv Mater* 34 (2022) e2200850.
- [45] E. Wachtel, I. Lubomirsky, The elastic modulus of pure and doped ceria, *Scr. Mater.* 65 (2011) 112–117.
- [46] F. Wang, F. Zeng, Z. Yu, C. Chen, X. Huang, W. Zhang, Y. Lan, J. Li, A comparative study about the influence of nitrogen doping and oxygen vacancies on the photocatalytic performance of ceria, *Surf. Interfaces* 46 (2024) 103889.
- [47] J. Ma, N. Xu, Y. Luo, Q. Liu, Y. Pu, Defect generation and morphology transformation mechanism of CeO₂ particles prepared by molten salt method, *Ceram. Int.* 49 (2023) 4929–4943.
- [48] Z. Li, L. Jin, Z. Cao, C. Zhang, X. Cao, G. Han, S. Peng, Y. Liu, Development and characterization of a novel RE³⁺-doped Core-shell CeO₂ abrasive system and its glass CMP investigations, *Appl. Surf. Sci.* 638 (2023) 158055.
- [49] L.D. Sonawane, A.S. Mandawade, L.N. Bhoye, H.I. Ahemad, S.S. Tayade, Y.B. Aher, A.B. Gite, L.K. Nikam, S.D. Shinde, G.H. Jain, G.E. Patil, M.S. Shinde, Sol-gel and hydrothermal synthesis of CeO₂ NPs: Their physicochemical properties and applications for gas sensor with photocatalytic activities, *Inorg. Chem. Commun.* 164 (2024) 112313.
- [50] Z. Kou, C. Wang, W. Zhou, A. Chen, Y. Chen, Trivalent lanthanum and ytterbium doped meso-silica/ceria abrasive systems toward chemical mechanical polishing (CMP) and ultraviolet irradiation-assisted photochemical mechanical polishing (PCMP), *Appl. Surf. Sci.* 657 (2024) 159733.
- [51] C. Alvarez-Galvan, P.G. Lustemberg, F.E. Oropeza, B. Bachiller-Baeza, M. Dapena Ospina, M. Herranz, J. Cebollada, L. Collado, J.M. Campos-Martín, V.A. de la Peña-O’Shea, J.A. Alonso, M.V. Ganduglia-Pirovano, Highly Active and Stable Ni/La-Doped Ceria Material for Catalytic CO₂ Reduction by Reverse Water-Gas Shift Reaction, *ACS Appl. Mater. Interfaces* 14 (2022) 50739–50750.
- [52] S.-K. Sun, L.M. Mottram, N.C. Hyatt, On the existence of the compound “Ce₃NbO⁷⁺” prepared under air atmosphere, *J. Rare Earths* 39 (2021) 596–599.
- [53] D. Sun, Y. Chen, X. Yu, Y. Yin, G. Tian, Engineering high-coordinated cerium single-atom sites on carbon nitride nanosheets for efficient photocatalytic amine oxidation and water splitting into hydrogen, *Chem. Eng. J.* 462 (2023) 142084.
- [54] M. Zhu, C. Zhao, X. Liu, X. Wang, F. Zhou, J. Wang, Y. Hu, Y. Zhao, T. Yao, L.-M. Yang, Y. Wu, Single Atomic Cerium Sites with a High Coordination Number for Efficient Oxygen Reduction in Proton-Exchange Membrane Fuel Cells, *ACS Catal.* 11 (2021) 3923–3929.
- [55] C. Ren, R. Yang, Y. Li, H. Wang, Modulating of facets-dependent oxygen vacancies on ceria and its catalytic oxidation performance, *Res. Chem. Intermed.* 45 (2019) 3019–3032.
- [56] L. Wang, G. Ren, W. Xie, J. Zhang, D. Pan, S. Wang, Simple and facile synthesis of single-crystal CeO₂ abrasives and its highly efficient removal mechanism on SiO₂ film, *Appl. Surf. Sci.* 654 (2024) 159510.
- [57] D. Chen, D. He, J. Lu, L. Zhong, F. Liu, J. Liu, J. Yu, G. Wan, S. He, Y. Luo, Investigation of the role of surface lattice oxygen and bulk lattice oxygen migration of cerium-based oxygen carriers: XPS and designed H₂-TPR characterization, *Appl. Catal. B* 218 (2017) 249–259.
- [58] P. Hu, Y. Chen, R. Sun, Y. Chen, Y. Yin, Z. Wang, Synthesis, characterization and frictional wear behavior of ceria hybrid architectures with 111 exposure planes, *Appl. Surf. Sci.* 401 (2017) 100–105.
- [59] I. Uslu, A. Aytimur, M.K. Öztürk, S. Koçyiğit, Synthesis and characterization of neodymium doped ceria nanocrystalline ceramic structures, *Ceram. Int.* 38 (2012) 4943–4951.
- [60] J. Paier, C. Penschke, J. Sauer, Oxygen defects and surface chemistry of ceria: quantum chemical studies compared to experiment, *Chem Rev* 113 (2013) 3949–3985.
- [61] X.A. Zhou, F. Zhang, X. Fu, N. Zhang, J. Huang, X. Cai, H. Ding, B. Li, L. Niu, S. Li, Utilizing fast ion conductor for single-crystal Ni-rich cathodes to achieve dual-functional modification of conductor network constructing and near-surface doping, *Energy Storage Mater.* 52 (2022) 19–28.
- [62] C. Chen, S. Yue, Y. Liu, H. You, Unveiling superior chemical mechanical polishing properties of a novel shell-core structure: Insights from an atomic-scale perspective, *Appl. Surf. Sci.* 672 (2024) 160845.
- [63] J. Cheng, S. Huang, X. Lu, Preparation of Surface Modified Ceria Nanoparticles as Abrasives for the Application of Chemical Mechanical Polishing (CMP), *ECS J. Solid State Sci. Technol.* 9 (2020) 024015.